nature communications

Article

https://doi.org/10.1038/s41467-026-72117-0

Enhancing gas sensing recyclability and recovery rate by crystal engineering of CuI motif in MOFs

Received: 18 July 2025

Accepted: 2 April 2026

Published online: 18 April 2026

Check for updates

Zi-Wei Li[1,7], Bin Tan[2,7], Xiu-Ze Hei[3], Xing-Wu Liu[4], Ke Zhao[2], Chuan-Zhe Wang[1], Ke-Feng Li[1], Yong-Jun Chen[1], Xiao-Ying Huang[1], Kui Tan[5], Zhao-Feng Wu[1] ✉, Jing Li[6] ✉ & Gang Xu[1] ✉

Metal-organic frameworks (MOFs) possess high sensitivity as chemiresistive gas sensing materials at room temperature (RT), while their applications are severely hampered by the issues of slow recovery and poor recyclability. To address these challenges, a strategy integrating DFT calculation with experimental synthesis is developed to identify and remove non-essential active units with excessive interactions to gas molecules, thereby enhancing sensing recovery and recyclability. In a case study, DFT calculations reveal that one-dimensional (1D) $\{Cu_4I_3\}_n^{n+}$ chains in a K-MOF, K-CuI-K-INA (HINA = isonicotinic acid), exhibit strong affinity to NO_2 while 2D $\{Cu_4I_5\}_n^{n-}$ layers show moderate interactions. Thus, by modulating the structure features of CuI motifs in M-CuI-K-INA (M = Na^+, K^+, and Cs^+, HINA = isonicotinic acid) type of MOFs, their NO_2 sensing recovering and recycling performances are consequently optimized. Particularly, Cs-CuI-K-INA with solely 2D $\{Cu_4I_5\}_n^{n-}$ layers possesses the best sensing recovery and recycle abilities, meanwhile maintains the excellent sensitivity and selectivity among these RT NO_2 sensing materials presented in the current study. This approach paves the way for chemiresistive sensing materials with improved recoverability and recyclability while retaining high sensitivity and selectivity.

Extensive studies have been conducted on chemiresistive sensing materials over the past decades[1–5]. Among them, metal-organic frameworks (MOFs), emerging as promising sensing materials capable of operating at room temperature (RT) with high selectivity and sensitivity, have drawn intense attention[6–10]. However, due to the excessive interactions between the sensing active site and target gas analyte, the reported MOF sensing materials commonly suffer from slow sensing recovery and poor recycling issues[11,12]. To overcome the aforementioned obstacles, during the gas-sensing tests, MOF sensing materials are often heated or exposed to light to facilitate the desorption of gas molecules[13,14]. Nevertheless, these approaches often result in compromised sensing sensitivity and increased sensing device complexity. Designing MOF sensing materials with intrinsic abilities in rapid recovery and good recyclability remains a critical challenge.

CuI moieties are recently proven to be promising building and active units for designing MOF gas sensing materials[15–17]. In our

[1]State Key Laboratory of Structural Chemistry, Fujian Provincial Key Laboratory of Materials and Techniques toward Hydrogen Energy, Fujian Institute of Research on the Structure of Matter, the Chinese Academy of Sciences, Fuzhou, Fujian, PR China. [2]School of Chemistry and Chemical Engineering, Beijing Institute of Technology, Beijing, PR China. [3]Hoffmann Institute of Advanced Materials, Shenzhen Polytechnic University, 7098 Liuxian Blvd, Nanshan District, Shenzhen, PR China. [4]Synfuels China Technology Co.Ltd., Leyuan Second South Street Yanqi Development Zone Huairou, Beijing, PR China. [5]Department of Chemistry, University of North Texas, Denton, TX, USA. [6]Department of Chemistry and Chemical Biology, Rutgers University, 123 Bevier Rd. Piscataway, NJ, USA. [7]These authors contributed equally: Zi-Wei Li, Bin Tan. ✉e-mail: zfwu@fjirsm.ac.cn; jingli@rutgers.edu; gxu@fjirsm.ac.cn

previous work, CuI-K-INA (HINA = isonicotinic acid), bearing the mixed one-dimensional (1D) $\{Cu_4I_3\}_n^{n+}$ chains and 2D $\{Cu_4I_5\}_n^{n-}$ layers, demonstrated good sensing sensitivity to NO_2[15]. Despite this, CuI-K-INA encountered slow sensing recovery and poor recycling issues, necessitating light irradiation to optimize its gas sensing performances[15]. Thus, CuI-K-INA is a good model material for developing an approach to identify and remove non-essential active motifs with excessive interactions to gas molecules, thereby enhancing recovery and recyclability for MOF sensing materials.

In this work, DFT calculations and experimental synthesis have been integrated to develop a crystal engineering strategy for optimizing gas sensing recovery and recyclability of MOF sensors (Fig. 1). This strategy helps to identify and eliminate non-essential active units having excessive interactions with gases. First of all, we used CuI-K-INA (presented as K-CuI-K-INA in this work for clearity) as a model material[15]. DFT calculation revealed that 1D α-$\{Cu_4I_3\}_n^{n+}$ chains (α and β was used to denote isomers) can excessively interact to NO_2 with an adsorption energy as high as −1.37 eV, while the 2D $\{Cu_4I_5\}_n^{n-}$ layers exhibit a comparatively moderate energy value of −1.18 eV (Fig S1). Secondly, the structures of CuI motifs in M-CuI-K-INA can be modulated by changing M^+ cations from Na^+, K^+, to Cs^+. Na-CuI-K-INA contains only 1D β-$\{Cu_4I_3\}_n^{+}$ chains, K-CuI-K-INA is composed of the mixed 1D α-$\{Cu_4I_3\}_n^{n+}$ chains and 2D $\{Cu_4I_5\}_n^{n-}$ layers, while Cs-CuI-K-INA contains solely $\{Cu_4I_5\}_n^{n-}$ layers. Consequently, the sensing recovery and recycling capacity for M-CuI-K-INA MOFs were greatly optimized. Particularly, Cs-CuI-K-INA showed the highest sensitivity, lowest limit-of-detection (LOD) value, and excellent recovery and recyclability among these M-CuI-K-INA MOFs, which are also comparable to the best-performing RT NO_2 sensing materials reported to date.

Results and Discussion

Structures Analysis

As documented in our former work, MOF of $[(Cu_9I_7)K_{10}(INA)_{12}(H_2O)]$ (named as K-CuI-K-INA in this work for a clearly comparative study), bearing 1D α-$\{Cu_4I_3\}_n^{n+}$ chains and 2D $\{Cu_4I_5\}_n^{n-}$ layers, exhibits an excellent chemiresistive sensing performance to NO_2 under light irradiation[15]. Thus, DFT calculations were conducted to better understand the structure-property relationship in this MOF. DFT calculations reveal that both the 1D chain-like and 2D layered CuI motifs can adsorb NO_2 through an endothermic process, with the 1D chains exhibiting a much higher absorption energy than the 2D layers (Fig. 2a and Fig S1). Consequently, while these abundant Cu(I) sites can enhance sensing sensitivity, they also indicate the recovery and recycling performances are compromised, as the absorbed NO_2 must be removed to re-expose the active Cu(I) sites for the next sensing cycle[15–19]. Therefore, finding an effective approach to remove the extra 1D α-$\{Cu_4I_3\}_n^{n+}$ chains while retain only the 2D $\{Cu_4I_5\}_n^{n-}$ layers in the K-CuI-K-INA framework would help optimize its sensing recovery and recycling capacity without sacrificing probing sensitivity. In K-CuI-K-INA, most K atoms show seven-coordinated modes, except for K4 which exhibits an eight-coordinated way (Fig S11-12). As a result, the INA ligands coordinated around K4 atoms follow an asymmetrical stacking arrangements above and below the $\{K\text{-}COO\}_n$ layer, leading to the generation of 1D α-$\{Cu_4I_3\}_n^{n+}$ chains and a 2D $\{Cu_4I_5\}_n^{n-}$ layer on each side of the K-INA layer (Fig. 2b and S2)[15].

Since alkali metals have different atomic radii and adopt various coordination modes, we found introducing hetero-metals to competitively coordinate with HINA can yield MOFs confining solely 1D CuI chain or 2D layer, offering an opportunity to investigate gas sensing performance based on structural features of CuI motifs. By introducing Cs^+ as a heteroatom, together with K^+ ions to competitively coordinate with HINA, a 3D MOF named as $[(Cs_{2.1}K_{7.9})(Cu_{10}I_8)(INA)_{12}]$ (Cs-CuI-K-INA) was obtained (Fig. 2c). Cs^+ ion has a larger radius and more coordiantion numbers than that of K^+, altering the coordiantion modes between K^+ and HINA ligand during the self-assembly[20–22]. Notably, Cs^+ ions only co-occupy the coordiantion sites of K^+, and their introduction alters the coordiantion numbers (seven to eight) of K^+ in K-CuI-K-INA into a solely seven-coordinated mode (Fig S13). As a reult, although HINA adopt varied spatial orientation to coordinate with the two metals (L1-L6), similar to those in K-CuI-K-INA, the INA- located above and below the K-COO layer form a symmetrical stacking arrangements. The pyridine rings in INA- ligands poking out on both sides of the layer are aligned nearly parallel to each other (Fig S14), leading to the formation of only 2D $\{Cu_4I_5\}_n^{n-}$ layers with the same structure as that in K-CuI-K-INA which are periodically confined into the resultant MOF of Cs-CuI-K-INA (Fig. 2c and S15).

While introducing Na^+ with comparatively small radius and few coordination numbers to competitively coordinate to INA- with K^+, a 3D MOF of Na-CuI-K-INA namely $\{(Na_2K_3)(Cu_4I_3)(INA)_6\}_n$ was generated. Similar to the functions of Cs^+, the introducing of Na^+ ions alters the coordination behaviors of K^+. In Na-CuI-K-INA, both Na^+ and K^+ coordinate independently to the carboxylic groups in INA^- ligands (Fig S16). The Na^+ ions adopt penta-coordination modes while K^+ ions possess hexa- or hepta-coordination spheres, which further bind to eight different COO- groups to form a $\{Na\text{-}K\text{-}COO\}_n$ layer (Fig S16a-c). Consequently, the pyridine rings in INA- ligands, which poke out on both sides of the layer and are aligned parallel among themselves and nearly parallel to the *b* axis, guide the formation of 1D chain-like structure assembled with $\{Cu_4I_3\}_n^{n+}$ segments that connected via single Cu-I bond (Fig. 2d). The 1D β-$\{Cu_4I_3\}_n^{n+}$ chains with the same formula as that in K-CuI-K-INA are strategically positioned within the confinement space created by pyridines in Na-CuI-K-INA (Fig S16d). Clearly,

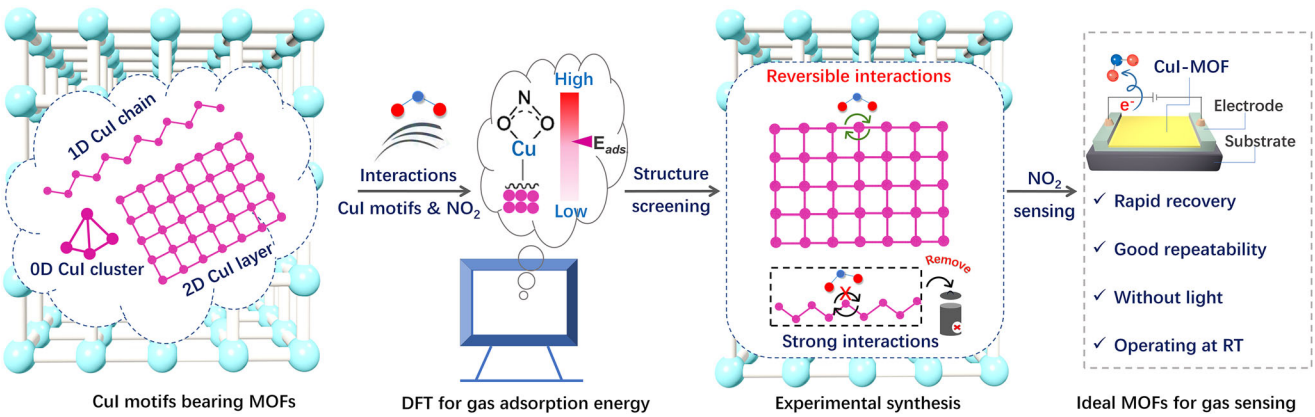

Fig. 1 | Diagrammatic representation of this study. Schematic illustration of integrating DFT calculation with crystal engineering strategy to tailor structures of CuI motifs in MOFs to optimize the NO_2 sensing recovery and cycling performances.

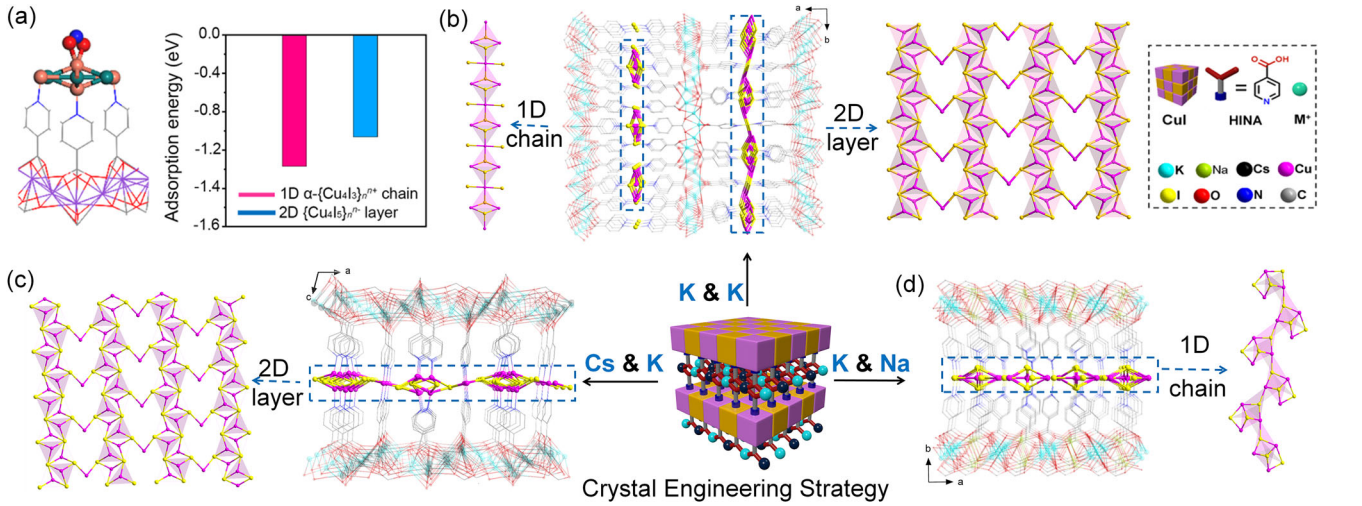

Fig. 2 | The illustration of integrating the DFT calculation with crystal engineering strategy to tailor the structure features of CuI motifs in M-CuI-K-INA. **a** Adsorption energy of NO_2 with CuI motifs in K-CuI-K-INA from DFT calculations. **b** K-CuI-K-INA bearing the mixed 1D α-$\{Cu_4I_3\}_n^{n+}$ chains and 2D $\{Cu_4I_5\}_n^{n-}$ layers viewed along c axis direction. **c** Cs-CuI-K-INA with solely 2D $\{Cu_4I_5\}_n^{n-}$ layer viewed along b axis direction. **d** Na-CuI-K-INA with only 1D β-$\{Cu_4I_3\}_n^{n+}$ chains viewed along the *c* axis direction.

introducing hetero-alkali metals to competitively coordinate with HINA can effectively guide the formation of the CuI motifs in MOFs with varied dimensionalities from 1D CuI chain to the 2D layer.

Physical characterizations

The purity of the crystal samples for M-CuI-K-INA are characterized by PXRD (Fig S5-8), EA, and ICP measurements. The electronic structures for M-CuI-K-INA were analyzed by DFT calculations (Fig S17-18). Taking Cs-CuI-K-INA as an example, the valance band maximum (VBM) is primarily composed of the atomic orbitals of the CuI motif (Cu 3 d and I 5p atomic orbitals), while the conduction band minimum (CBM) is contributed predominately by the organic INA^- ligand (2p orbitals of C, N and O). This result indicates that while Cs^+ plays an important role in tailoring the dimensionality of CuI in Cs-CuI-K-INA, it is essentially not involving in tuning the band structures (Fig S17). The optical absorption spectra for these CuI-bearing MOFs are well within the visible light region with estimated band gaps around 2.1 eV ~ 2.5 eV, lower than that of the pristine CuI (Fig S19-20)[23–25]. Additionally, these compounds exhibit excellent thermal stability with decomposition temperatures as high as >300 °C (Fig S9-10).

As both Na-CuI-K-INA and Cs-CuI-K-INA feature rod-like crystal morphology with minimeter (mm) size, we investigated their anisotropic characteristics in electrical conductivity using a direct current two-terminal method on the selected single crystals (Fig S21-23). The as-made Na-CuI-K-INA and Cs-CuI-K-INA exhibit an obvious anisotropic conductivity under the same measuring conditions. For example, the single crystal of Cs-CuI-K-INA exhibits a conductivity of 2.81×10^{-10} S/cm measured along the short side of the rod sample at RT (the direction parallel to the *c* axis of the single crystal structure, Fig S22), while the conductivity measured along the long side of the single crystal (within the 2D-CuI layer of crystal structure viewed along *a* axis, Fig S23) is one order of magnitude higher, 1.18×10^{-9} S/cm. This is reasonable as the conductivity within the extended 2D inorganic layer in Cs-CuI-K-INA is significantly higher than that out of the 2D layer[26,27]. With the measuring temperature increased to 413 K, the conductivities reach to the highest values of 1.70×10^{-8} and 0.60×10^{-6} S/cm measured along the *c* and *a* axis of the single crystal, respectively (Fig S23). The conductivity value of 0.60×10^{-6} S/cm is comparable to that of $Cu_4I_6(bttmp)_2$ (2.8×10^{-6} S/cm)[28] and K-CuI-K-INA (1.21×10^{-6} S/cm) [15].

The good linearity of Lnσ to 1000/T confirms their semiconducting nature (Fig S24-25). For example, Cs-CuI-K-INA exhibits a temperature dependent conductivity, which could reach to a magnitude of 10^{-8} S/cm with the temperature increasing to 393 K, three magnitude orders of enhanced conductivity compared with that of 10^{-11} S/cm measure at RT (Fig S25). This result demonstrates a typical Arrhenius-type behavior and can be explained by charge transport generating from the thermal activation conduction processes[29–31]. Moreover, the Mott–Schottky test was also performed on Cs-CuI-K-INA, as a representative compound, at 1000, 1500, and 2500 Hz, Fig S26. In the Mott–Schottky plot, the C^{-2} value has a negative slope to the potential, while the intersection with the x-axis is independent of frequency, indicating Cs-CuI-K-INA is a typical p-type semiconductor[29,30]. Moreover, the ultraviolet photoelectron spectroscopy (UPS) measurement shows that the Fermi level of Cs-CuI-K-INA deviate from the middle of the band gap and are close to the valence band (VB), which further suggests Cs-CuI-K-INA is p-type semiconducting material (Fig S27)[31].

Gas sensing performances

K-CuI-K-INA bearing the mixed 1D CuI chains and 2D layers demonstrated excellent NO_2 sensing performances but required photo-excitation[15]. Through removing the 1D CuI chains of high affinity with NO_2 molecules by a crystal engineering strategy, Cs-CuI-K-INA presented in this work exhibits an optimized sensing performances without light irradiation. As shown in Fig. 3a, Cs-CuI-K-INA shows an excellent chemiresistive sensing behavior to NO_2 with high selectivity over other interference gases. The conductance of Cs-CuI-K-INA shows an obvious increase upon exposure to NO_2 and drops back to the initial value when purged with dry air (Fig. 3b). The average response ($R_{average}$) of five individually as-made sensing devices to 10 ppm NO_2 is up to 649% (Fig. 3b and S28a).

The sensing sensitivity for Cs-CuI-K-INA is at least orders of magnitude greater than that of the pristine CuI which had to be activated at 240 °C[32,33]. As depicted in Fig. 3c, after removing the 1D chain-like CuI motifs, Cs-CuI-K-INA exhibits a typical dynamic response-recovery curves to NO_2 with a broad 1–100 ppm concentration range, giving a better sensing repeatability with a CV value of 2.20% (Fig S28b). The low CV value highlights its exceptional sensing repeatability and reliability. In contrast, K-CuI-K-INA containing the mixed 1D CuI chains and 2D layers and Na-CuI-K-INA bearing solely 1D CuI chains displayed significantly larger response CV of 13.25% and 14.30%, respectively, over the same number of cycles, indicating their relatively poorer repeatability and reliability (Fig. 3c and S29).

https://doi.org/10.1038/s41467-026-72117-0

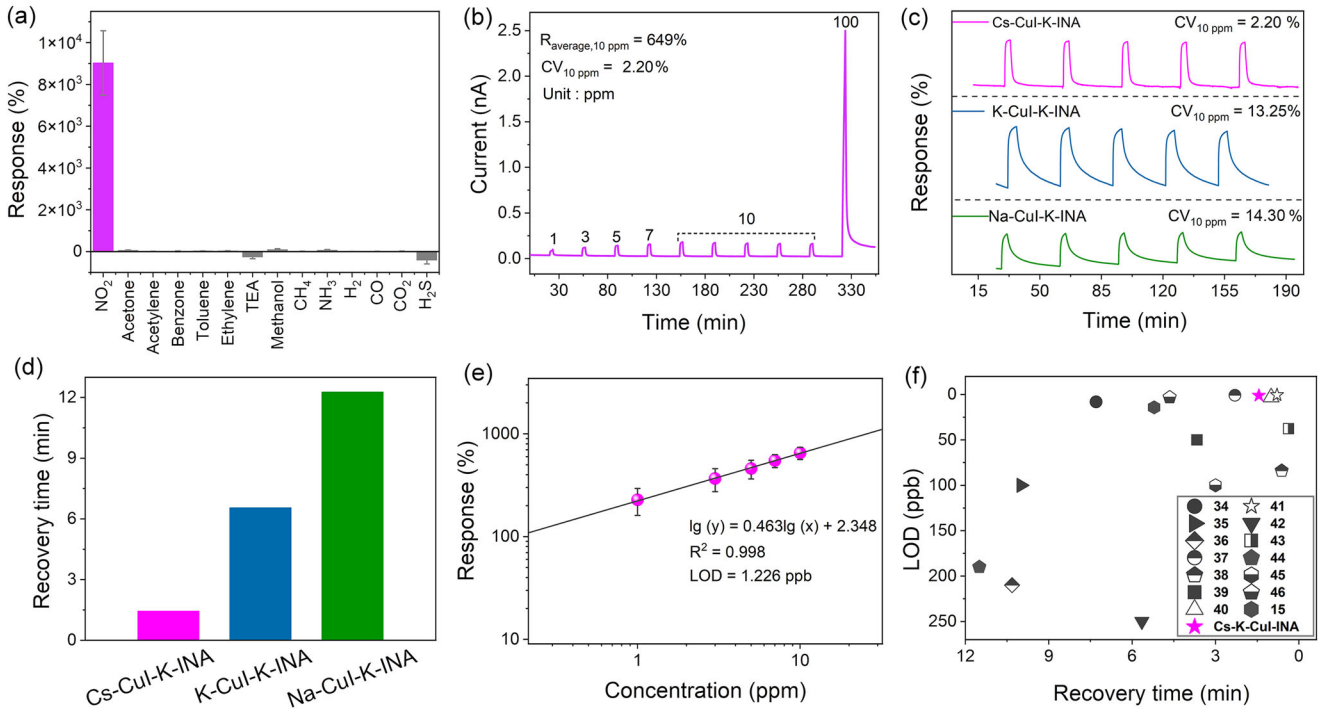

Fig. 3 | Characterization of gas sensing performance. a Responses of Cs-CuI-K-INA to 100 ppm NO_2 comparing with that of other interference gases. **b** Response and recovery curve of Cs-CuI-K-INA towards NO_2 with different concentrations at RT. **c** Coefficient of variation for cycle testing of M-CuI-K-INA (M = Na, K and Cs) towards 10 ppm NO_2. **d** Sensing recovery time of M-CuI-K-INA (M = Na, K and Cs). **e** Log−Log linear fitting of the response-concentration plot. **f** Response time and LOD values of Cs-CuI-K-INA in comparison with the excellent NO_2 RT sensing materials reported to date (without light, with LOD values < 250 ppb and recovery time <700 s). Error bars present the standard deviation of the mean of three experiments. Source data are provided as a Source Data fle.

The fast recovery time is also a very important parameter concerning sensing performances. At the dark condition, Cs-CuI-K-INA has the recovery time of 1.44 min, which is ~1/4 of that of K-CuI-K-INA (6.55 min). The recovery time for Cs-CuI-K-INA is even only 1/3 of that of K-CuI-K-INA (3.54 min) under light irradiation[15], demonstrating the faster sensing recovery performances of Cs-CuI-K-INA (Fig. 3d and S28c). The observed differences in CV values and sensing recovery time of K-CuI-K-INA, as compared to our previous study[15], may be attributed to batch-to-batch variability in sample preparation and discrepancies in the operational parameters of the sensing instruments. In contrast, Na-CuI-K-INA shows the slowest recovery time (Fig. 3d, e, S29c and S30).

The theoretical limit of detection (LOD) of Cs-CuI-K-INA can be calculated to be about 1.226 ppb from the simulated linear equation by setting the response to 10% (Fig. 3e), which is comprable to that of K-CuI-K-INA[15]. This result indicates the strategy presented here can improve gas sensing recovering and recycling performances without sacrificing sensing sensitivity[15]. The LOD is comparable to the best sensing materials including but not limited to metal oxides, chalcogenides and MOFs sensing materials (Fig. 3f)[34–46]. More details of the related sensing parameters, including $R_{average}$, CV and LOD values, of other NO_2 sensing materials are listed in Table S4 for a comprehensive comparison. When considering performance parameters such as recovery capability, response time, and LOD value, Cs-CuI-K-INA stands out as one of the satisfactory RT chemresistive NO_2 sensing materials reported to date. Cs-CuI-K-INA maintains its stability across a broad range of solvents, demonstrating its potential applicability in real-world applications (Fig S31). It exhibits a consistent and reliable sensing response to 10 ppm NO_2 over duration of two months, thereby confirming its long-term stability in sensing performance (Fig S32). The sensing response to NO_2 under different relative humidity (RH) levels and mixed gas conditions shows negligible variation (Fig S33-34). Moreover, its significantly enhanced and scalable yield, achieved through the optimization of synthesis parameters (Fig S35), further supports its potential for practical applicability in NO_2 sensing.

Mechanism studies

Time-resolved diffuse reflectance infrared fourier transform spectroscopy (DRIFTS) measurements were performed to elucidate the sensing mechanism. As depicted in Fig. 4a, a series of new peaks were observed for Cs-CuI-K-INA after exposed to NO_2 with respect to the spectrum of the pristine sample. The intensities of these bands continue to increase as a function of exposing time, indicating that they correspond to the species resulting from NO_2 interaction/reaction on the sample surface[47–51]. The molecularly adsorbed NO_2 was detected by monitoring its ν_{as} band at 1730 cm^{-1}, which shows a large upward (blue-) shift compared to its gas phase value at 1620 cm^{-1}[47]. Such blue-shift was also observed in former studies of NO_2 adsorption on cationic surfaces and can be attributed to the partial electron donation from antibonding orbitals to the surface, thus stiffening N = O bond and raising its frequency[52–56]. Nitrate species (NO_3^-), as a result of disproportionation reaction of NO_2[15,18,19], was also observed as typifed by the growth of their characteristic bands labeled as I, II, and III, which are assigned to the N = O stretching and the asymmetric/symmetric stretching vibrations of $-NO_2$ within NO_3^- ions[57,58]. A noticeably large separation between I and II suggests a possible bridging or chelating nitrate complex on the surface of the compound through bidentate bonding configuration was formed, which is in accordance with the DFT calcualtion results for NO_2 adsorption with a bidentate O,O′-nitrito binding way as a favorable adsorption mode (Fig S1)[57,59]. NO is characterized by the broad band around 1800 − 1900 cm^{-1}, which corresponds to its stretching vibration of nitrosyl species formed on the cationic sites[56], and N_2O is characterized by N − O stretching modes around 1300 − 1200 cm^{-1}. However, they grow in a proportional manner with NO_3^- bands demonstrating they are the reaction products of NO_2 with Cs-CuI-K-INA. XPS measurments also provide evidence for

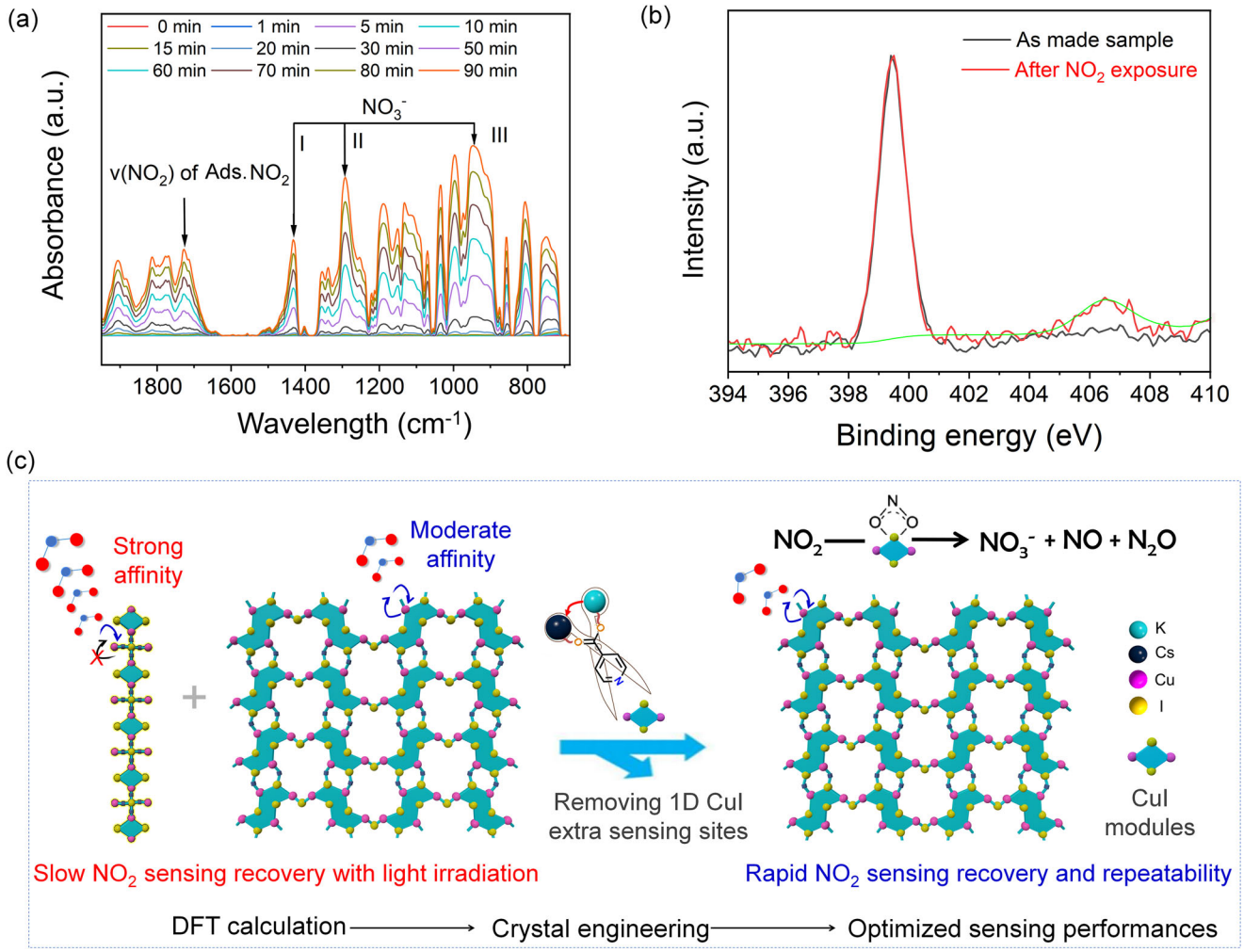

Fig. 4 | Characterization for the NO_2 sensing mechanism and illustration of structure-property relationship. a Time-resolved DRIFTS difference spectra of Cs-CuI-K-INA exposing at NO_2 atmosphere. **b** XPS spectra of N1s in Cs-CuI-K-INA before and after NO_2 exposure. **c** The schematic summarizing the structure-sensing performance relationship.

the presence of these adsorbed species, as indicated by the spectrum of N1*s* which shows two peaks around 400 and 407 eV after exposing to NO_2. The peak around 400 eV is due to the N of INA ligand while 407 eV is typically ascribled to surface NO_3^- ions (Fig. 4b)[58]. It may also involve the electrons transfer between the molecularly adsorbed NO_2 and the host Cs-CuI-K-INA structure[60]. The ν_{as} band for the adsorbed NO_2 was not observed for the sample after gas sensing measurements, indicating NO_2 adsorbed on the sample surface can be removed to achieve sensing repeatability (Fig S36). Moreover, the PXRD measurements of the sample after NO_2 sensing confirmed that the structures remain unchanged, suggesting good resuability of these samples (Fig S5 and S7). As seen in Fig S37, the N_2 adsorption measurement on the powdered Cs-CuI-K-INA sample indicates that the sample is non-porous. This result confirms the sensing occurs on the external surfaces, not in the internal structure of the materials[61–63]. Based on the results discussed above, the NO_2 sensing process can be viewed as a Lewis acid−base interaction between the Cu(I) site and NO_2, which invovles the electrons transfer between the highly acidic NO_2 and CuI motifs in MOFs then resulted in resistance change (Fig. 4c) [15,18,19].

DFT calculations were also conducted to better understand the inner relationship between structure and sensing performances. In K-CuI-K-INA, NO_2 prefers to interat with Cu(I) atoms on the Cu(I) centers in both 1D chains and 2D layers with a bidentate O,O′-nitrito binding mode (Fig S1)[18,19]. This finding is consistent with the superior sensing response of K-CuI-K-INA compare to that of Cs-CuI-K-INA containing only 2D CuI layered motifs (Fig. 3b)[15]. However, the release of NO_2 adsorbed onto both the 1D chain-like and 2D layered CuI motifs in K-CuI-K-INA is more challenging than for the solely 2D CuI layers in Cs-CuI-K-INA, resulting in a slower sense recovery. Thus, light irradiation was necessary to enhance its recovery capacity[13–15]. By adopting both Cs^+ and K^+ ions to competitively coordinate with HINA, the 1D CuI chains in K-CuI-K-INA were removed, leaving only 2D $\{Cu_4I_5\}_n^{n-}$ layers confined within the framework of Cs-CuI-K-INA (Fig. 4c). After removing the 1D chains, the adsorption energy of NO_2 to CuI motifs in Cs-CuI-K-INA is reduced to -1.07 eV, while the energy for the 1D CuI chains that confined in Na-CuI-K-INA is increased to -1.64 eV (Fig S38). A Bader charge analysis also reveals the reduced charge transfer observed in 2D $\{Cu_4I_5\}_n^{n-}$ layers, suggesting the moderate interactions between the layered CuI modules and NO_2 (Fig. 4c and S39). The conductivity of Cs-CuI-K-INA exhibited a more pronounced and accelerated increase upon exposure to NO_2 compared to K-CuI-K-INA, which is consistent with the results obtained from the DFT calculations (Fig S40)[15]. Consequently, without light irradation, the recovery time for Cs-CuI-K-INA (1.44 min) is shortened to 1/4 of that for K-CuI-K-INA, which can also be reduced to nearly 1/3 of that for K-CuI-K-INA (3.54 min) even with light assistance[15]. The low CV value of 2.20% for Cs-CuI-K-INA highlights its exceptional sensing repeatability and reliability by removing the 1D CuI chains with excessive interactions to NO_2 (Figs. 3c and 4c). These results aforementioned above demonstrate that removing non-essential active units with excessive

interactions to gas molecules can benefit the sensing response and recyclability to the sensing materials. The alteration in resistance observed in conventional sensing materials upon exposure to gas molecules is typically attributed to the chemisorption and subsequent reaction of these molecules on the surface of the sensing element. Nevertheless, the application of external stimuli such as temperature or light is often required to address the challenges associated with low sensitivity, limited selectivity, and irreversibility in gas sensing performance (Table S4)[13,14,64]. MOFs have been developed to operate at RT with abundant reaction sites on the surface, but they also encounter the challenge of irreversible NO_2 detection resulting from the formation of a stable coordination complex[65,66]. In this work, by integrating DFT calculations, the crystal engineering approach we established represents a promising method for tailoring the structural characteristics of sensing modules. This, in turn, facilitates the optimization of gas sensing recovery and recyclability of MOF sensors (Fig. 4c). We intend to extend this approach into a general strategy for tailoring the structural properties of conventional inorganic materials—including metal oxides, metal halides, and sulfides—to significantly enhance their sensing performances.

In this work, we first carried out DFT calculations to show that compared to the 2D layers, the 1D CuI chains interact more strongly with NO_2 molecules, resulting in slow gas sensing recovery and poor recyclability of K-CuI-K-INA (the model MOF). We then introduced alkali-metals (Na^+ and Cs^+) as hetero-atoms which leads to Na-CuI-K-INA and Cs-CuI-K-INA, composed of only 1D CuI chains and 2D layers, respectively. By removing the 1D α-$\{Cu_4I_3\}_n^{n+}$ chains with excessive NO_2 adsorption energy, Cs-CuI-K-INA bearing solely 2D $\{Cu_4I_5\}_n^{n-}$ layers as active NO_2 sensing motifs demonstrates enhanced sensing performance with faster recovery and better recyclability than those of K-CuI-K-INA and Na-CuI-K-INA. This work offers a valuable insight into the molecular level design of chemiresistive materials by integrating DFT calculation with crystal engeering stratedy to optimize and enhance their chemiresistive sensing performances.

Methods

Characterizations

All the chemicals were used without further purification. Elemental analyses (EA) of C, H, and N were performed using a German Elementary Vario EL III instrument. UV-Vis absorbance photometric tests were carried out on a UV-2600 and PerkinElmer Lambda 350 UV-Vis spectrophotometer at RT in the range of 200–800 nm. Solid-state optical diffuse reflectance spectra were recorded on a Shimadzu 2600 UV/vis spectrometer at RT in the range of 200–800 nm. A $BaSO_4$ plate was utilized as a standard which possesses 100% reflectance. The absorption data were then obtained from the reflectance spectra by using the Kubelka-Munk function $\alpha/S = (1-R)^2/2R$, where α refers to the absorption coefficient, S refers to the scattering coefficient, and R refers to the reflectance. Thermogravimetric analyses (TGA) were carried out on a NETZSCH STA449C unit at a heating rate of 5 °C/min under nitrogen atmosphere. The powder X-ray diffraction (PXRD) patterns were obtained from a Miniflex II diffractometer at 30 kV and 15 mA using Cu *Kα* (1.54178 Å) in the angular range of 2θ = 3-65° at RT. The PXRD analyses were conducted on a Rigaku Smartlab X-ray diffractometer with Cu Kα1 radiation (λ = 1.5406 Å) at a scanning speed of 5° min^{-1}. The surface chemical analysis was investigated by X-ray photoelectron spectroscopy (XPS) on a Thermo Scientific ESCALAB 250 Xi XPS system. The metal elemental ratios were determined by ICP-atomic emission spectrometry (AES) using an Ultima 2 instrument. Inductively coupled plasma-optical emission spectroscopy. N_2 adsorption isotherm was measured on a ASAP (Accelerated Surface Area and Porosimetry) 2020 System at 77 K. Mott–Schottky was performed on a IMS Electrochemistry workstation-disk electrode. The data of ultraviolet photoelectron spectroscopy (UPS) was collected from a Thermo Scientific ESCALAB 250 Xi XPS system (monochromatic Al K*α* X-rays (1486.6 eV) operating at 15 kV; the base pressure: 5.0×10^{-8} Pa). The samples were first dried in a vacuum oven for 8 h before test.

Starting Materials

NaI (99%, Macklin Inc.), CsI (99%, Adamas Reagent Co., Ltd), KI (99 %, Adamas Reagent Co., Ltd), CuI (99%, Adamas Reagent Co., Ltd), 4-Picolinic acid (99%, Adamas Reagent Co., Ltd). All the chemicals were purchased from commercial sources and used without any further purification.

Synthesis of Na-CuI-K-INA

A mixture of CuI (100 mg), NaI (75 mg), KI (75 mg), INA (100 mg), 3.0 mL DMF, 2.0 mL CH_3CN and 2.0 mL ethanol was sealed in 20 mL vessel, heated at 100 °C for 6 days, and then cooled to room temperature. The reaction yielded ~50 mg red block-like crystal. The yield was 24.8% based on Cu element. EA, Calcd. for $C_{36}H_{24}Cu_4I_3K_3Na_2N_6O_{12}$: C, 28.25%; H, 1.58%; N,5.49%; found: C, 28.57%; H, 1.50%; N, 5.50%; ICP, Calcd. for $C_{36}H_{24}Cu_4I_3K_3Na_2N_6O_{12}$: Cu, 16.61%; K, 7.66%; Na, 3.00%; found: Cu, 17.08%; K, 7.67%; Na, 3.08%.

Synthesis of Cs-CuI-K-INA

Cs-CuI-K-INA could be synthesized using the same procedure as Na-CuI-K-INA except that 75 mg of CsI instead of NaI was used in the reaction. The reaction yielded ~40 mg yellow rod-like crystals. The yield was 20.3% based on Cu element. Crystals exhibiting high yields were also successfully synthesized by combining CuI (500 mg), CsI (750 mg), KI (750 mg), and INA (500 mg) in a solvent mixture consisting of 15.0 mL DMF, 10.0 mL CH_3CN, and 10.0 mL ethanol. The mixture was sealed in 40 mL vessel, heated at 100 °C for 6 days, and then cooled to room temperature. ~468 mg crystal samples were collected and the yield was 47.5% based on Cu element. EA, Calcd. for $C_{36}H_{24}Cs_{1.25}Cu_5I_4K_{3.75}N_6O_{12}$: C, 23.11%; H, 1.29%; N, 4.49%; Found: C, 23.36%; H, 1.27%; N, 4.48%; ICP, Calcd. for $C_{36}H_{24}Cs_{1.25}Cu_5I_4K_{3.75}N_6O_{12}$: Cu, 16.98%; K, 7.83%; Cs, 8.88%; found: Cu, 17.61%; K, 7.53%; Cs (This element cannot be tested in the lab).

Electrical conductivity tests

Electrical conductivity (σ) was obtained by fitting the linear region of the current–voltage curves to Ohm's law. For the bulk sample measurements, two-contact probe method was used. The single crystal electrodes were made using silver paste and 50 μm gold line by placing the crystal between two electrodes and connected to the semiconductor analysis system (4200SCS, Keithley). The electrical conductivity of the sample was calculated based on Ohm's law. The tests were performed under dark conditions (without any light source), and the temperature change was controlled by the gas sensing station.

Gas Sensing Measurements

10 mg sample was grinded and dispersed in ethanol solution. Then, 20 μL as made sample suspension was directly drip-coated on the interdigital electrode. The electrode was then dried at 60 °C under vacuum for 6 h before sensing test. The sensing characterization was conducted on a home-made system reported in previous work[67]. The constant gas flow was 600 mL min^{-1}, the bias on the sensor was set to be 5 V and the current data were recorded using a Keithley 2602B Sourcemeter. Gases with accurate concentration were generated by mixing target gases with dry air in a certain ratio via mass flow controllers (CS-200C, Beijing Sevenstar Qualiflow Electronic Equipment Manufacturing Co., Ltd., China) and then injected into a quartz tube. Responsivity (*R*): It assesses the influence of NO_2 on responses ($\Delta I/I_0$, I_0 is the current in air and ΔI represents the change in current in the circuit after exposure to the analyte gas). The coefficient of variation (CV) was estimated by $R_{SD}/R_{avg} \times 100\%$, where R_{SD} and $R_{average}$. are the standard deviation (SD) and the average value of responses. The

response and recovery times were acquired as the times taken to achieve 90% of the total resistance change.

Time-resolved in-situ DRIFTS spectra collection

DRIFTS spectra were collected on a Nicolet 6700 FT-IR spectrometer with MCT/A detector cooled by liquid nitrogen. Data collection was performed on OMNIC software. The KBr was heated to 100 °C under a stream of dry synthetic air for 2 h, after which the sample cup was cooled to room temperature and purged with dry synthetic air. After that, a raw absorbance spectrum was collected as background. The sample was processed with the same procedure except NO_2 was used throughout the test. All spectra were obtained by scanning with a resolution of 4 cm^{-1} from 650 to 2000 cm^{-1}.

X-ray Crystallography

Single-crystal X-ray diffraction data of Na-CuI-K-INA were collected on SuperNova Oxford diffractometer with graphite monochromated Mo$K\alpha$ radiation (λ = 0.71073 Å). Single crystal data of Cs-CuI-K-INA was collected on MM007-Saturn724 with Mo$K\alpha$ radiation at 293(2) K. The structures were solved by direct methods and refined by full-matrix least-squares on F^2 using the SHELX-2015 program[68]. Non-hydrogen atoms were refined with anisotropic displacement parameters and the hydrogen atoms bonded to C and N atoms were positioned with idealized geometry. The empirical formulae were confirmed by EA. Detailed crystallographic data and structure-refinement parameters are summarized in Table S1. Table S2 lists important bond distances.

Density functional theory (DFT) calculations

All the DFT calculations were performed by using the Vienna ab initio simulation package VASP[69,70]. The projector augmented wave method was used to describe the interaction between ions and electrons. Electron-electron exchange and correlation interactions are described by using the Perdew-Burke-Ernzerhof functional (PBE) within the generalized gradient approximation (GGA)[71]. A plane wave basis set with a cutoff energy of 400 eV and a k-point grid generated by the Monkhorst-Pack method were found to give converged results for the surface calculations. The structures were relaxed using either the conjugate gradient algorithm or the quasi-Newton scheme until the forces on all unfixed atoms were less than 0.01 eV/Å. To investigate NO_2 adsorption configurations on K-CuI-K-INA and Na-CuI-K-INA and Cs-CuI-K-INA in this work, we constructed slab models with CuI exposure, as shown in the Fig S1 and S30. The atoms of the MOFs and the adsorbate (NO_2) were allowed to relax. It should be noted that the energies of all configurations presented in this work include corrections for dispersion (D3) and zero-point energy (ZPE). To describe the interaction between the adsorbate and the substrate, the adsorption energy was defined as Eads = E(adsorbate/slab) - E(adsorbate) - E(slab) where E(slab), E(adsorbate) and E(adsorbate/slab) represent the energies of optimized slab, gas-phase adsorbate and adsorbate-slab complex, respectively. The spin-polarization calculation was considered in gas species and adsorption systems with open shell character. According to the above definition, a negative value indicated that the process is exothermic, whereas positive values are for endothermic processes.

Data availability

Additional methods and data are provided in the Supplementary Information. All data are available within the paper and its Supplementary Information. Source data are provided with this paper.

References

1. Barsan, N., Koziej, D., Weimar, U. J. S. & Chemical, A. B. Metal oxide-based gas sensor research: How to? *Sens. Actuators B Chem.* **121**, 18–35 (2007).
2. Kaushik, A. et al. Organic–inorganic hybrid nanocomposite-based gas sensors for environmental monitoring. *Chem. Rev.* **115**, 4571–4606 (2015).
3. Anichini, C. et al. Chemical sensing with 2D materials. *Chem. Soc. Rev.* **47**, 4860–4908 (2018).
4. Chowdhury, M. & Oehlschlaeger, M. Artificial intelligence in gas sensing: a review. *ACS Sens.* **10**, 1538–1563 (2025).
5. Bulemo, P. et al. Selectivity in chemiresistive gas sensors: strategies and challenges. *Chem. Rev.* **125**, 4111–4183 (2025).
6. Oprea, A., Bârsan, N. & Weimar, U. Work function changes in gas sensitive materials: Fundamentals and applications. *Sens. Actuators B Chem.* **142**, 470–493 (2009).
7. Yuan, H.-Y., Li, N.-X., Fan, W.-D., Cai, H. & Zhao, D. Metal-organic framework based gas sensors. *Adv. Sci.* **9**, 2104374 (2022).
8. Peng, X.-Y., Wu, X.-H., Zhang, M.-M. & Yuan, H.-Y. Metal–organic framework coated devices for gas sensing. *ACS Sensors* **8**, 2471–2492 (2023).
9. Sharma, A. et al. Porous materials as effective chemiresistive gas sensors. *Chem. Soc. Rev.* **53**, 2530–2577 (2024).
10. Yao, M.-S., Li, W.-H. & Xu, G. Metal–organic frameworks and their derivatives for electrically-transduced gas sensors. *Coord. Chem. Rev.* **426**, 213479 (2021).
11. Meng, Z., Aykanat, A. & Mirica, K. A. Welding metallophthalocyanines into bimetallic molecular meshes for ultrasensitive, low-power chemiresistive detection of gases. *J. Am. Chem. Soc.* **141**, 2046–2053 (2019).
12. Aykanat, A., Meng, Z., Stolz, R. M., Morrell, C. T. & Mirica, K. A. Bimetallic two-dimensional metal–organic frameworks for the chemiresistive detection of carbon monoxide. *Angew. Chem. Int. Ed.* **61**, e202113665 (2022).
13. Xu, F. & Ho, H. P. Light-activated metal oxide gas sensors: a review. *Micromachines* **8**, 333 (2017).
14. Kumar, R., Liu, X., Zhang, J. & Kumar, M. Room-temperature gas sensors under photoactivation: from metal oxides to 2D materials. *Nanomicro Lett.* **12**, 164 (2020).
15. Wu, Z.-F. et al. Confinement of 1D chain and 2D layered CuI modules in K-INA-R frameworks via coordination assembly: structure regulation and semiconductivity tuning. *J. Am. Chem. Soc.* **145**, 19293–19302 (2023).
16. Mishra, S., Patel, C., Pandey, D., Mukherjee, S. & Raghuvanshi, A. Semiconducting 2D Copper(I) iodide coordination polymer as a potential chemiresistive sensor for methanol. *Small* **20**, 2311448 (2024).
17. Pandey, D., Patel, C., Mishra, S., Mukherjee, S. & Raghuvanshi, A. Semiconducting 2D Copper(I) framework for Sub-ppb-level ammonia sensing. *ACS Appl. Nano Mater.* **7**, 15833–15840 (2024).
18. Timmons, A. J. & Symes, M. D. Converting between the oxides of nitrogen using metal–ligand coordination complexes. *Chem. Soc. Rev.* **44**, 6708–6722 (2015).
19. Wright, A. M., Sun, C.-Y. & Dincă, M. Thermal cycling of a MOF-Based NO disproportionation catalyst. *J. Am. Chem. Soc.* **143**, 681–686 (2021).
20. Forgan, R. S. et al. Nanoporous carbohydrate metal–organic frameworks. *J. Am. Chem. Soc.* **134**, 406–417 (2012).
21. Patel, H. A. et al. Noninvasive substitution of K^+ sites in cyclodextrin metal–organic frameworks by Li^+ ions. *J. Am. Chem. Soc.* **139**, 11020–11023 (2017).
22. Wang, P., Lin, J.-W., Guo, Z. & Mao, L.-L. Impact of Alkali Metal Coordination on the Photoluminescence Quantum Efficiency Trend in Hybrid Supramolecular Trimetallic Halides. *Chem. Mater.* **36**, 10651–10660 (2024).
23. Gao, P., Gu, M., Liu, X., Zheng, Y.-Q. & Shi, E. -w Crystal growth and luminescence properties of CuI single crystals. *Optik* **125**, 1007–1010 (2014).

24. Li, M.-C., Zhang, Z., Zhao, Q., Huang, M. & Ouyang, X. Electronic structure and optical properties of doped γ-CuI scintillator: a first-principles study. *RSC Adv.* **13**, 9615–9623 (2023).
25. Pishtshev, A. & Karazhanov, S. Z. Structure-property relationships in cubic cuprous iodide: A novel view on stability, chemical bonding, and electronic properties. *J. Chem. Phys.* **146**, 064706 (2017).
26. Mohammadpour, A., Farsinezhad, S., Wiltshire, B. D. & Shankar, K. Majority carrier transport in single crystal rutile nanowire arrays. *Phys Status Solidi Rapid Res. Lett.* **8**, 512–516 (2014).
27. Wang, S.-J. et al. A phase transformable ultrastable titanium-carboxylate framework for photoconduction. *Nat. Commun.* **9**, 1660 (2018).
28. Zhu, K. et al. A New Type of Hybrid Copper Iodide as Nontoxic and Ultrastable LED Emissive Layer Material. *ACS Energy Lett.* **6**, 2565–2574 (2021).
29. Huang, Y.-L., Chiu, S.-P., Zhu, Z.-X., Li, Z.-Q. & Lin, J.-J. Variable-range-hopping conduction processes in oxygen deficient polycrystalline ZnO films. *J. Appl. Phys.* **107**, 063715 (2010).
30. Lien, C.-C., Wu, C.-Y. & Lin J-J, L.iZ. -Q. Electrical conduction processes in ZnO in a wide temperature range 20–500 K. *J. Appl. Phys.* **110**, 063706 (2011).
31. Li, Y. et al. Coordination assembly of 2D ordered organic metal chalcogenides with widely tunable electronic band gaps. *Nat. Commun.* **11**, 261 (2020).
32. Wolpert, B., Leitl, M., Pfitzner, A. & Mirsky, V. M. Chemosensitive properties of electrically conductive Cu(I) compounds at room temperature. *Sens. Actuators B Chem.* **134**, 839–842 (2008).
33. Wolpert, B., Wolfbeis, O. S. & Mirsky, V. M. Gas sensing properties of electrically conductive Cu(I) compounds at elevated temperatures. *Sens. Actuators B Chem.* **142**, 446–450 (2009).
34. He, L., Zhang, W.-Y., Wu, H.-Y. & Zhao, Y. Zn–Co Zeolitic Imidazolate Framework Nanoparticles Intercalated in Graphene Nanosheets for Room-Temperature NO_2 Sensing. *ACS Appl. Nano Mater.* **4**, 3998–4006 (2021).
35. Koo, W.-T. et al. Few-Layered WS_2 Nanoplates Confined in Co, N-Doped Hollow Carbon Nanocages: Abundant WS_2 Edges for Highly Sensitive Gas Sensors. *Adv. Funct. Mater.* **28**, 1802575 (2018).
36. Chen, P. et al. Two-Dimensional Conjugated Metal-Organic Frameworks with Large Pore Apertures and High Surface Areas for NO_2 Selective Chemiresistive Sensing. *Angew. Chem. Int. Ed.* **62**, e202306224 (2023).
37. Jiang, H.-J. et al. Organic "receptor" fully covered few-layer organic–metal chalcogenides for high-performance chemiresistive gas sensing at room temperature. *Chem. Commun.* **56**, 5366–5369 (2020).
38. Liu, H. et al. Physically Flexible, Rapid-Response Gas Sensor Based on Colloidal Quantum Dot Solids. *Adv. Mater.* **26**, 2718–2724 (2014).
39. Kumar, R., Jenjeti, R. N. & Sampath, S. Two-Dimensional, Few-Layer $MnPS_3$ for Selective NO_2 Gas Sensing under Ambient Conditions. *ACS Sens.* **5**, 404–411 (2020).
40. Geng, X. et al. Atomically dispersed Pb ionic sites in PbCdSe quantum dot gels enhance room-temperature NO_2 sensing. *Nat. Commun.* **12**, 4895 (2021).
41. Wen, Y.-Y. et al. A covalent organic–inorganic hybrid superlattice covered with organic functional groups for highly sensitive and selective gas sensing. *Angew. Chem. Int. Ed.* **60**, 19710–19714 (2021).
42. Qiang, X.-Y. et al. Effect of the functionalization of porous silicon/WO_3 nanorods with Pd nanoparticles and their enhanced NO_2-sensing performance at room temperature. *Materials* **11**, 764 (2018).
43. Bai, H.-N. et al. A room-temperature chemiresistive NO_2 sensor based on one-step synthesized SnO_2 nanospheres functionalized with Pd nanoparticles and rGO nanosheets. *Appl. Surf. Sci.* **575**, 151698 (2022).
44. Li, P.-P. et al. Sequential ligand exchange of coordination polymers hybridized with in situ grown and aligned Au nanowires for rapid and selective gas sensing. *ACS Appl. Mater. Interfaces* **11**, 13624–13631 (2019).
45. Rui, K. et al. Dual-function metal–organic framework-based wearable fibers for gas probing and energy storage. *ACS Appl. Mater. Interfaces* **10**, 2837–2842 (2018).
46. Geng, X. et al. Photoexcited NO_2 enables accelerated response and recovery kinetics in light-activated NO_2 gas sensing. *ACS Sens.* **6**, 4389–4397 (2021).
47. Tan, K. et al. Interaction of acid gases SO_2 and NO_2 with coordinatively unsaturated metal organic frameworks: M-MOF-74 (M = Zn, Mg, Ni, Co). *Chem. Mater.* **29**, 4227–4235 (2017).
48. Pietrogiacomi, D., Campa, M. C., Ardemani, L. & Occhiuzzi, M. Operando FTIR study of Fe-MOR, Co-MOR, and Ni-MOR as catalysts for simultaneous abatement of NO_x and N_2O with CH_4 in the presence of O_2. An insight on reaction pathway. *Catal. Today* **336**, 131–138 (2019).
49. Kang, J. et al. Time-resolved in situ visualization of the structural response of zeolites during catalysis. *Nat. Commun.* **11**, 5901 (2020).
50. Hadjiivanov, K. I. et al. Power of infrared and Raman spectroscopies to characterize metal-organic frameworks and investigate their interaction with guest molecules. *Chem. Rev.* **121**, 1286–1424 (2021).
51. Qu, W.-Y. et al. NO selective catalytic reduction over atom-pair active sites accelerated via in situ NO oxidation. *Environ. Sci. Technol.* **57**, 7858–7866 (2023).
52. Aylor, A. W., Larsen, S. C., Reimer, J. A. & Bell, A. T. An infrared study of NO decomposition over Cu-ZSM-5. *J. Catal.* **157**, 592–602 (1995).
53. A. W. Aylor LJL, J. A. Reimer & A. T. Bell. An infrared study of NO reduction by CH4 over Co-ZSM-5, *Vol. 101*, Elsevier, pp 661-670, (1996).
54. Hadjiivanov, K., Klissurski, D., Ramis, G. & Busca, G. Fourier transform IR study of NO_x adsorption on a CuZSM-5 $DeNO_x$ catalyst. *Appl. Catal. B* **7**, 251–267 (1996).
55. Hadjiivanov, K. I. IR study of CO and NO_x sorption on Ag-ZSM-5. *Micropor. Mesopor. Mater.* **24**, 41–49 (1998).
56. Hadjiivanov, K. I. Identification of Neutral and Charged N_xO_y Surface Species by IR Spectroscopy. *Catal. Rev.* **42**, 71–144 (2000).
57. Nakamoto K. In Handbook of Vibrational Spectroscopy (2001)
58. Jensen, S. et al. Porous Ti-MOF-74 Framework as a Strong-Binding Nitric Oxide Scavenger. *J. Am. Chem. Soc.* **142**, 16562–16568 (2020).
59. Koupepidou, K. et al. One atom can make all the difference: gas-induced phase transformations in bisimidazole-linked diamondoid coordination networks. *J. Am. Chem. Soc.* **145**, 10197–10207 (2023).
60. Rosseler, O. et al. Chemistry of NO_x on TiO_2 Surfaces Studied by Ambient Pressure XPS: Products, Effect of UV Irradiation, Water, and Coadsorbed K^+. *J. Phys. Chem. Lett.* **4**, 536–541 (2013).
61. Xu, P.-C., Xu, T., Yu, H. & Li, X.-X. Resonant-Gravimetric Identification of Competitive Adsorption of Environmental Molecules. *Analy. Chem.* **89**, 7031–7037 (2017).
62. Lv, Y.-Q., Yu, H.-T., Xu, P.-C., Xu, J.-Q. & Li, X.-X. Metal organic framework of MOF-5 with hierarchical nanopores as micro-gravimetric sensing material for aniline detection. *Sens. Actuators B Chem.* **256**, 639–647 (2018).
63. Gong, W., Pan, Y., Shi, Y., Wang, G. & Xu, G. Imidazole-amino modified organic-metal chalcogenide for enhanced recyclability and recovery rate in gas sensing. *Sens. Actuators B Chem.* **445**, 138577 (2025).
64. Khan, M. A. H., Rao, M. V. & Li, Q. Recent Advances in Electrochemical Sensors for Detecting Toxic Gases: NO_2, SO_2 and H_2. *S. Sensors* **19**, 905 (2019).
65. Jo, Y.-M. et al. Visible-Light-Activated Type II Heterojunction in Cu_3(hexahydroxytriphenylene)$_2$/Fe_2O_3 Hybrids for Reversible NO_2 Sensing: Critical Role of π–π* Transition. *ACS Central Sci.* **7**, 1176–1182 (2021).

66. Yan, X.-L. et al. Redox Synergy: Enhancing Gas Sensing Stability in 2D Conjugated Metal–Organic Frameworks via Balancing Metal Node and Ligand Reactivity. *Angew. Chem. Int. Ed.* e202408189 (2024).
67. Yao, M.-S., Tang, W.-X., Wang, G.-E., Nath, B. & Xu, G. MOF thin film-coated metal oxide nanowire array: significantly improved chemiresistor sensor performance. *Adv. Mater.* **28**, 5229–5234 (2016).
68. Sheldrick, G. Crystal structure refinement with SHELXL. *Acta Crystallogr. C Struct. Chem.* **71**, 3–8 (2015).
69. Kresse, G. & Furthmuller, J. Efficiency of ab-initio total energy calculations for metals and semiconductors using a plane-wave basis set. *Comput. Mater. Sci.* **6**, 15–50 (1996).
70. Kresse, G. & Furthmuller, J. Efficient iterative schemes for ab initio total-energy calculations using a plane-wave basis set. *Phys. Rev. B* **54**, 11169–11186 (1996).
71. Grimme, S., Antony, J., Ehrlich, S. & Krieg, H. A Consistent and Accurate ab Initio Parametrization of Density Functional Dispersion Correction (DFT-D) for the 94 Elements H-Pu. *J. Chem. Phys.* **132**, 154104 (2010).

Acknowledgements

B.T. acknowledges support from the National Natural Science Foundation of China (22305019). Z.W. acknowledges support from the National Natural Science Foundation of China (No. 22175178). G.X. acknowledges support from the National Natural Science Foundation of China (Nos. 91961115, 22171263, 62227815), Scientific Research and Equipment Development Project of CAS (YJKYQ20210024), Fujian Science & Technology Innovation Laboratory for Optoelectronic Information of China (2021ZR130 and 2021ZR101) and the Natural Science Foundation of Fujian Province (2021J01513, 2021J02017). J.L. acknowledges the partial support from U.S. Department of Energy, Office of Science, Office of Basic Energy Sciences under Award No. DE-SC0019902.

Author contributions

The manuscript was written through contributions of all authors. Z.W., J.L., and G.X. conceived the project and revised the manuscript. Z.L. designed and performed most of the experiments and analyzed the data. B.T. offered help in data analyses and written parts of this manuscript. X.H. and Y.C. provided help in text modification. X.L. and K.Z. conducted the DFT calculations. C.W., K.L., and K.T. offered help in the partial experiments and data analysis. X.H. solved the single crystal data.

Competing interests

The authors declare no competing interests.

Additional information

Supplementary information The online version contains supplementary material available at https://doi.org/10.1038/s41467-026-72117-0.

Correspondence and requests for materials should be addressed to Zhao-Feng Wu, Jing Li or Gang Xu.

Peer review information *Nature Communications* thanks Himanshu Aggarwal, Hongye Yuan and the other, anonymous, reviewer(s) for their contribution to the peer review of this work. A peer review file is available.